ROYAL SOCIETY
OF CHEMISTRY

PAPER

Check for updates

Electronic quenching of sulfur induced by argon collisions

David M. G. Williams, [ID] *[a] Nicole Weike, [ID] [b] Manuel Lara, [ID] [c]
Kevin M. Dunseath [ID] [a] and Alexandra Viel [ID] [a]

An accurate potential energy model, explicitly designed for studying scattering and treating the spin–orbit and nonadiabatic couplings on an equal footing, is proposed for the S + Ar system. The model is based on the Effective Relativistic Coupling by Asymptotic Representation (ERCAR) approach, building the geometry dependence of the spin–orbit interaction *via* a diabatisation scheme. The resulting full diabatic model is used in close-coupling calculations to compute inelastic scattering cross sections for de-excitation from the $S(^1D_2)$ fine structure level into the ^3P multiplet. The energy grid is tuned to resolve the many resonances present and to guarantee converged thermal rates from 1 to 300 K. At temperatures above 100 K, the computed thermal rate coefficients for quenching of $S(^1D_2)$ are in good agreement with results from an earlier experimental and theoretical study. The branching ratio at 296 K for de-excitation into the $S(^3P_0)$ level agrees well with the value obtained by a different experiment. A discrepancy however remains between theory and experiment at lower temperatures. This is discussed in light of the interference mechanisms at play during this quenching process.

I. Introduction

The de-excitation (quenching), or removal of electronically excited atoms and molecules plays a key role in the chemical evolution of gaseous environments such as planetary atmospheres, combustion engines, and the interstellar medium. It can also have a sometimes undesirable effect in more controlled environments such as atomic and molecular beam experiments. Due to their low reactivity, noble gases such as helium and argon are often used as carriers of other atomic and molecular species that are the actual subjects of the study. In spite of this, they can significantly quench the population of excited states before the process of interest can occur. In particular, sulfur in its $S(^1D)$ excited state has received much attention in beam experiments since the 1970's.[1,2] The rate coefficient for the removal of $S(^1D)$ by Ar, determined by Black and Jusinski,[3] was 1.4×10^{-11} cm³ molecule⁻¹ s⁻¹, of the same order of magnitude as the net removal by reaction and quenching combined in collisions with H₂ (2.1×10^{-11} cm³ molecule⁻¹ s⁻¹). However, the removal rate corresponding to helium is 3 orders of magnitude smaller than that for argon. For this reason, helium

rather than argon was chosen as the carrier gas in a subsequent experiment analyzing the reactive collision $S(^1D) + H_2 \rightarrow SH + H$ using the CRESU (Cinétique de Réaction en Ecoulement Supersonique Uniforme or Reaction Kinetics in a Uniform Supersonic Flow) technique.[4] A later experiment by the same group investigated specifically the quenching of $S(^1D)$ by collisions with argon for a wider range of temperatures.[5] They found in particular a rate coefficient of 1.78×10^{-11} cm³ molecule⁻¹ s⁻¹ at 300 K, slightly larger than the value proposed by Black and Jusinski.[3] While all these studies provided total rate coefficients, Stout *et al.*[6] were able to deduce the fine-structure distribution of the quenched sulfur atoms by argon using time-resolved coherent anti-Stokes Raman spectroscopy (CARS), concluding that approximately 80% of the total $S(^3P)$ yield is produced in the $^3P_0$ level.

The experimental work on quenching of $S(^1D)$ by argon reported by Lara *et al.*[5] was accompanied by a theoretical study based on close-coupling calculations with the aim of understanding further the dynamics involved. The theoretical rate coefficients obtained are in good agreement with the experimental results at higher temperatures, but overestimate them at lower temperatures. At 5.8 K for example, the theoretical rate is a factor two larger than the experimental one. It is interesting to note that similar discrepancies between theory and experiment are seen in recent studies on the electronic quenching of $O(^1D)$ in collisions with noble gases.[7–9] In particular, for the case of O + Ar, the differences are also of the order of a factor of two, not just at low temperatures but throughout the range from 50 to 350 K. Implementation details of the scattering

[a] *Univ Rennes, CNRS, IPR (Institut de Physique de Rennes) – UMR 6251, F-35000 Rennes, France. E-mail: david.williams@univ-rennes.fr*
[b] *Theoretische Chemie, Universität Bielefeld, Postfach 100131, D-33501 Bielefeld, Germany*
[c] *Departamento de Química Física Aplicada, Facultad de Ciencias, Universidad Autónoma de Madrid, 28049 Madrid, Spain*

simulations notwithstanding, we infer that the differences between theory and experiment for these chemically very similar systems are likely caused by results being extremely sensitive to the underlying potential energy curves. Indeed, for S + Ar, Lara *et al.*[5] attributed this discrepancy to the interference mechanism underlying the process. In simple terms, the quenching process can be understood as probability transfers (jumps) localized around crossing points of the various potential curves and in particular those correlating with S(^{1}D) and S(^{3}P). The system traverses the crossings twice, once when the atoms are approaching and once when they are receding (having been reflected by the repulsive barrier). This creates two portions of flux which have travelled along different paths and hence have different phases. The resulting interference produces oscillations in the quenching probability as a function of the energy, known as Stückelberg oscillations.[10] In the S + Ar system, there are crucial avoided crossings whose intrinsic interference mechanism makes the theoretical results extremely sensitive to any small change in the position of these crossings. This poses a stringent test for any theoretical simulation of this kind of process: any small inaccuracy in the potential energy curves will have a radical effect in the interference pattern and hence in the scattering simulation. Determining the curve crossings with an accuracy of a few cm^{-1}, particularly challenging at crossings in the repulsive walls, was therefore deemed necessary in order to better reproduce this quantum interference process. This stringent dependence on the quality of the *ab initio* computation motivates us to use the Effective Relativistic Coupling by Asymptotic Representation (ERCAR) approach to reinvestigate the electronic quenching of S by Ar. Indeed the ERCAR scheme is one of the rare approaches for building accurate potential energy surface (PES) models that treat vibronic and spin–orbit coupling on an equal footing. Furthermore, the PES is furnished in a form suitable for scattering studies, as demonstrated in a recent application to the collisions of H with I.[11,12]

This paper is organized as follows. In Section II, the theoretical background is given while Section III provides the computational details. The coupled potential curves thus obtained are presented in Section IV A, and the results of the scattering computations are discussed in Section IV B. Finally, this work is summarized in Section V.

II. Theory

A. Theory for the potential energy surface

The potential energy surfaces (PESs) are developed within the Effective Relativistic Coupling by Asymptotic Representation (ERCAR) approach[13–18] to accurately account for the spin–orbit (SO) effect of a relativistically-treated atom within a molecule. The approach utilizes the idea that SO coupling is an atom-based effect. The full molecular Hamiltonian is thus represented in a diabatic asymptotic direct product basis composed of states of the relativistic atom and the remaining molecular fragment. In the following, the key ideas of the approach are given briefly.

The molecular electronic Hamiltonian $\hat{H}_e$ can be separated into the Coulomb Hamiltonian $\hat{H}_c$, which also contains all scalar relativistic effects, and the SO Hamiltonian $\hat{H}_{SO}$ as

$$\hat{H}_e = \hat{H}_c + \hat{H}_{SO}. \tag{1}$$

In general, the diabatic asymptotic basis $\{\psi_k^d(Q)\}$ is defined as direct products of atomic states $\psi_{k_2}^{at}$ of the relativistic atom and fragment states $\psi_{k_1}^{frag}(Q)$

$$\psi_k^d(Q) = \psi_{k_1}^{frag}(Q) \otimes \psi_{k_2}^{at}, \tag{2}$$

where Q represents the internal coordinates of the fragment. In the present case, $\psi_{k_2}^{at}$ describes the sulfur atom while the molecular fragment is just the argon atom, so that the fragment states $\psi_{k_1}^{frag}(Q)$ here do not depend on Q.

The molecular electronic Hamiltonian $\hat{H}_e$ is represented in the basis (2) and the matrix elements $W_{jk}^d(Q, R)$ of the resulting diabatic model read

$$
\begin{aligned}
W_{jk}^d(Q, R) &= \left\langle \psi_j^d(Q) \middle| \hat{H}_e(Q, R) \middle| \psi_k^d(Q) \right\rangle \\
&= \underbrace{\left\langle \psi_j^d(Q) \middle| \hat{H}_c(Q, R) \middle| \psi_k^d(Q) \right\rangle}_{W_{jk}^c(Q, R)} \\
&\quad + \underbrace{\left\langle \psi_{j_2}^{at} \middle| \hat{H}_{SO} \middle| \psi_{k_2}^{at} \right\rangle}_{H_{jk}^{SO} = \text{const.}},
\end{aligned}
\tag{3}
$$

where R is the fragment-atom distance. Hence, the diabatic model is split into the geometry dependent Coulomb Hamiltonian model, $\mathbf{W}^c(Q,R)$, and the geometry independent SO model, $\mathbf{H}^{SO}$. The SO model is a constant matrix which only depends on the atomic states of the relativistic atom.

In the determination of the SO model, the following effective n-electron SO operator is applied to the diabatic basis states,

$$\hat{H}_{SO} = \sum_{i_2, j_2} \hat{P}_{i_2} \hat{P}_{j_2} \left(\lambda_{i_2 j_2} \sum_{k=1}^{n} \hat{l}_k \cdot \hat{s}_k \right), \tag{4}$$

where $\hat{l}_k$ is the orbital angular momentum operator, $\hat{s}_k$ is the spin operator, and both act on each electron k. There are two atomic state projectors ($\hat{P}_{i_2}$ and $\hat{P}_{j_2}$) to account for both intra-state SO coupling for couplings within a single atomic multiplet and for inter-state SO coupling for couplings between different atomic terms of the same electron configuration. Both projectors act on the basis function to ensure that the operators $\hat{l}_k \cdot \hat{s}_k$ act on the intended atomic states of the relativistic atom. The $\lambda_{i_2 j_2}$ are the respective coupling constants for the intra-state and the inter-state SO coupling.

More details on the ERCAR approach can be found for example in ref. 16. The particular expressions for the geometry dependent Coulomb and the (geometry independent) SO model are system dependent. The details for the S + Ar system, where R is the sole internal coordinate, are given in Section III.

This journal is © the Owner Societies 2025

Phys. Chem. Chem. Phys., 2025, **27**, 3722–3731 | **3723**

B. Theory of scattering

We use the close-coupling formalism for an atomic collision of the type A + B given by Launay,[19] as summarized in ref. 12. The total Hamiltonian for the system may be written as

$$\hat{H} = -\frac{\hbar^2}{2\mu}\frac{1}{R}\frac{\partial^2}{\partial R^2}R + \frac{\hat{\ell}^2}{2\mu R^2} + \hat{V}(R) \qquad (5)$$

where R is the inter-nuclear distance, μ is the reduced mass of the system, $\hat{\ell}$ is the orbital angular momentum operator for the relative motion of the two atoms and $\hat{V}(R)$ denotes the electronic Hamiltonian. The solution of the corresponding Schrödinger equation is expanded in terms of partial waves $|\psi^{JM_J}\rangle$, which are eigenstates of the operators $\hat{J}^2$ and $\hat{J}_z$ for the total angular momentum J. These partial waves are further expanded in terms of space-fixed basis functions, eigenstates of $\hat{j}_{AB}^2$, $\hat{\ell}^2$ as well as $\hat{J}^2$ and $\hat{J}_z$, where j_{AB} denotes the angular momentum obtained by coupling the individual angular momenta j_A and j_B of atoms A and B:

$$|\psi^{JM_J}\rangle = \sum_\nu |\nu JM_J\rangle \frac{1}{R}F_\nu^J(R), \qquad (6)$$

where the index ν represents the ensemble of quantum numbers (γ, j_{AB}, ℓ), and γ labels the different asymptotic energy levels. The total angular momentum is then $\hat{J} = \hat{j}_{AB} + \hat{\ell}$. Substituting this expansion into the Schrödinger equation and projecting onto a particular basis function yields a set of coupled second-order differential equations for the radial basis functions in matrix form,

$$\frac{d^2}{dR^2}\mathbf{F}^J(R) + \mathbf{W}^J(R)\mathbf{F}^J(R) = 0, \qquad (7)$$

where $\mathbf{W}^J$ contains matrix elements of the electronic Hamiltonian and the centrifugal potentials in the different channels. These equations are solved for each total angular momentum J and at each collision energy. At a sufficiently large inter-atomic distance, where the off-diagonal elements of the coupling matrices vanish, the radial functions $\mathbf{F}^J$ expressed in the space fixed frame are rewritten as linear combinations of the regular and irregular spherical Bessel functions. The collisional matrix $\mathbf{K}^J$ is then obtained by matching the logarithmic derivative matrix $(\mathbf{F}^J)'(\mathbf{F}^J)^{-1}$ of the propagated solutions to that of the asymptotic forms, where the prime denotes differentiation with respect to R.

The partial integral cross section for a transition from level γ to level γ' for a given J, averaged over initial states and summed over final states, is given by

$$\sigma_{\gamma\gamma'}^J = \frac{\pi\hbar^2}{2\mu E_\gamma g_\gamma}(2J+1)\sum_{j_{AB}\ell;j'_{AB}\ell'}\left|T_{\gamma j_{AB}\ell;\gamma'j'_{AB}\ell'}^J\right|^2, \qquad (8)$$

where $g_\gamma = (2j_A(\gamma)+1)(2j_B(\gamma)+1)$ and E_γ is the collision energy relative to the initial level γ. In this equation, the transition matrix $\mathbf{T}^J = \mathbf{1} - \mathbf{S}^J$ is related to $\mathbf{K}^J$ by

$$\mathbf{T}^J = -2i\mathbf{K}^J(\mathbf{1} - i\mathbf{K}^J)^{-1}.$$

The total integral cross section $\sigma_{\gamma\gamma'}^{\text{tot}}$ is then obtained by summing the partial cross sections over all values of the total angular momentum J. Energy-dependent rate coefficients may also be defined as

$$k_{\gamma\gamma'}(E_\gamma) = v\sigma_{\gamma\gamma'}(E_\gamma) \quad \text{with} \quad v = \sqrt{2E_\gamma/\mu}. \qquad (9)$$

To compare with the experimental results, it is necessary to introduce thermal rates. Collisional rate coefficients $k_{\gamma\gamma'}(T)$ at temperature T for a transition from level γ to level γ' are given by averaging the integral cross section $\sigma_{\gamma\gamma'}^{\text{tot}}$ over a Maxwellian distribution:

$$k_{\gamma\gamma'}(T) = \left(\frac{8}{\pi\mu}\right)^{1/2}\left(\frac{1}{k_BT}\right)^{3/2}\int_0^\infty dE\, E\, \sigma_{\gamma\gamma'}^{\text{tot}}(E)\exp\left(-\frac{E}{k_BT}\right), \qquad (10)$$

where k_B is the Boltzmann constant.

III. Computational details

A. Ab initio computations

The ERCAR approach requires an ensemble of adiabatic electronic energies against which the model is fitted. These SO-free Coulombic energies were obtained in a two-step procedure combining complete active-space self-consistent field (CASSCF) calculations with multi-reference configuration interaction (MRCI) calculations with Davidson corrections (MRCI+Q) to properly capture the multi-configurational character of the states of interest. All calculations were performed in C_{2v} symmetry using the MOLPRO software package.[20] After testing both larger and smaller basis sets, the aug-cc-pV5Z orbital basis was found to be optimal in terms of accuracy *versus* CPU time and was used for *ab initio* data generation. Calculations were performed along the S–Ar distance comprising 520 data points lying between 3.9 and 1890 bohr (1000 Å). A fine grid is used for distances below 15 bohr, with a higher density of points in the interaction region and repulsive walls, so that 75% of the points lie below 7.6 bohr. Nine adiabatic energies were computed per point, which converge asymptotically to 3 distinct energy levels. From the components of the ^3P ($^3\Sigma^-$, $^3\Pi$), ^1D ($1^1\Sigma^+$, $^1\Pi$, $^1\Delta$) and ^1S ($2^1\Sigma^+$) states of sulfur, a total of 15 fine structure states of the composite system can be formed. Note that although the ^1S ($2^1\Sigma^+$) state lies much higher in energy, it is necessary to include it in order to have all states corresponding to the $[Ne]3s^23p^4$ ground configuration of sulfur.

Molecular orbitals and reference wave functions were first computed by state-averaged CASSCF calculations for each data point. The active space includes the 3p orbitals of sulfur. The orbitals were diabatized for each data point with respect to a reference calculation performed at a large S–Ar separation (1890 bohr). These diabatic orbitals then form the one-electron basis in the MRCI calculations in which the 3s and 3p orbitals of both sulfur and argon were used in the active space. Correlation and Davidson correction energies were rescaled by a factor of 1.123 for the lowest-lying triplet and singlet curves to maximally resemble a CCSD(T) reference coupled cluster calculation.

3724 | *Phys. Chem. Chem. Phys.*, 2025, **27**, 3722–3731

This journal is © the Owner Societies 2025

B. Diabatic Coulomb Hamiltonian model

In the following we describe the Coulomb part of the diabatic model Hamiltonian. Without spin–orbit coupling, the model is most easily expressed in terms of a basis of a 9×9 diabatic model reproducing the SO-free adiabatic energies. The diabatic state basis order is taken to be $^3\Sigma^-$, $^3\Pi$, $1^1\Sigma^+$, $^1\Pi$, $^1\Delta$, $2^1\Sigma^+$ throughout this section, and also specified in Table 1. All distances are given in bohr. As in ref. 11, the nuclear configuration space is split into three overlapping domains, henceforth called the repulsion domain $\mathcal{D}_R$ ($R \leq 10.8$), the dispersion domain $\mathcal{D}_D$ ($R \geq 15.1$) and the interaction domain $\mathcal{D}_I$ ($7.4 \leq R \leq 19$). Each diabatic matrix element is modelled by a sum of twice differentiable domain-specific functions, constructed such that their contributions vanish exactly outside of their respective domain. In other words, each diabatic matrix element $W_{jk}(R)$ (where j,k range from 1 to 9) can be expressed as

$$W_{jk}(R) = W_{jk}^R(R) + W_{jk}^I(R) + W_{jk}^D(R) \tag{11}$$

where

$$\forall R \notin \mathcal{D}^X : W_{jk}^X(R) = 0, \quad X \in \{R, I, D\}. \tag{12}$$

To ensure eqn (12) holds, we employ a switching function defined by

$$s(x) = \begin{cases} 0 & x \leq 0 \\ 6x^5 - 15x^4 + 10x^3 & 0 \leq x \leq 1 \\ 1 & x \geq 1 \end{cases} \tag{13}$$

In the present case, the matrix $W(R)$ has only one symmetry-allowed diabatic coupling element between $1^1\Sigma^+$ and $2^1\Sigma^+$ (states 4 and 9). This coupling term is of course vanishing at infinite separation of the two atoms, resulting in a diagonal $W(R)$ matrix for large enough values of R. The diagonal matrix elements are modelled as

$$W_{jj}^D(R) = s\left(\chi^D(R)\right)\frac{c_{6j}^D}{R^6} \tag{14}$$

where

$$\chi^D(R) = \frac{R - R_0^D}{R_1^D - R_0^D}. \tag{15}$$

This ansatz is exact in the asymptotic limit of $R \to \infty$ because both Ar and S are neutral atoms. Since the adiabatic and diabatic representations coincide for $R > 19$ bohr, c_{6j}^D was obtained via a linear fit against ab initio data on a double logarithmic scale, confirming the asymptotic behavior. We verified that no additional orders are needed in this dispersion domain to properly reproduce the ab initio data. $\chi^D(R)$ serves to shift and scale the distance coordinate R such that the contribution of the dispersion term vanishes for $R \leq R_0^D = 15$ bohr whereas $W_{jj}^R(R)$ and $W_{jj}^I(R)$ vanish for $R \geq R_1^D = 9$ bohr. The functions used for the diagonal matrix elements in the repulsion domain are similar but less constrained in their functional form. They are given by

$$W_{jj}^R(R) = \left(1 - s\left(\chi_j^R(R)\right)\right)\sum_{n=6}^{13}\frac{c_{nj}^R}{R^n} \tag{16}$$

where, similar to $\chi^D(R)$, $\chi_j^R(R)$ is defined by

$$\chi_j^R(R) = \frac{R - R_{0j}^R}{R_{1j}^R - R_{0j}^R}. \tag{17}$$

By construction $W_{jj}^R(R)$ vanishes for all $R \geq R_{1j}^R$, where R_{1j}^R depends on the particular state j, as given in Table 1. The diagonal functions in the interaction domain are defined such that they vanish at each domain boundary and are given by

$$W_{jj}^I(R) = s\left(\chi_j^R(R)\right)\left(1 - s\left(\chi^D(R)\right)\right)\sum_{n=6}^{12}\frac{c_{nj}^I}{R^n}. \tag{18}$$

Finally, the lone diabatic coupling element ($j \neq k$) is modelled similarly, but adding an exponential term for both interaction and repulsion domains:

$$W_{jk}^R(R) = \left(1 - s\left(\chi_j^R(R)\right)\right)\left(\alpha^R \exp\left(\beta^R R\right) + \sum_{n=6}^{j}\frac{d_n^R}{R^n}\right) \tag{19}$$

$$W_{jk}^I(R) = s\left(\chi_j^R(R)\right)\left(1 - s\left(\chi^D(R)\right)\right)\left(\alpha^I \exp\left(\beta^I R\right) + \sum_{n=6}^{j}\frac{d_n^I}{R^n}\right). \tag{20}$$

As stated above, $W_{jk}^D(R) = 0$.

All parameters for the repulsion and interaction domains have been obtained using a Levenberg–Marquardt fitting algorithm. Since only two states are coupled, most could be directly fitted against ab initio data. The coupled 2×2 sub-block describing the $^1\Sigma^+$ states had to be diagonalized before fitting.

C. Spin–orbit model

The model contains 15 basis states corresponding asymptotically to the atomic states ^3P, ^1D and ^1S of sulfur and ^1S of argon. The SO matrix is easily expressed in the basis of the four-electron Slater determinant spinors corresponding to each of the 3 states of sulfur considered here. The basis definition is given in Table 2. In this basis, the SO matrix can be written in

Table 1 Switching function parameters for each of the components $j = 1$ through 9 of the SO-free interaction potentials. Note that the switching function parameters $R_0^D = 15$ bohr and $R_1^D = 19$ bohr are identical for the 9 components

S	Symmetry	j	R_{0j}^R	R_{1j}^R
^3P	$^3\Sigma^-$	1	9.26	10.77
	$^3\Pi$	2–3	8.88	10.02
^1D	$1^1\Sigma^+$	4	7.37	8.13
	$^1\Pi$	5–6	9.35	10.02
	$^1\Delta$	7–8	9.35	10.02
^1S	$2^1\Sigma^+$	9	7.37	8.13

This journal is © the Owner Societies 2025

Phys. Chem. Chem. Phys., 2025, **27**, 3722–3731 | **3725**

Table 2 Quantum numbers of the 15 basis states used in the final diabatic full model. For convenience of the reader the quantum numbers of Ar are listed even if they are all null. Blank lines separate the different multiplets ^3P, ^1D and ^1S

Basis number	L_S	S_S	L_{Ar}	S_{Ar}	j_S	j_{Ar}	j_{SAr}	$M_{j_{SAr}}$
1	1	1	0	0	2	0	2	−2
2	1	1	0	0	2	0	2	−1
3	1	1	0	0	2	0	2	0
4	1	1	0	0	2	0	2	1
5	1	1	0	0	2	0	2	2
6	1	1	0	0	1	0	1	−1
7	1	1	0	0	1	0	1	0
8	1	1	0	0	1	0	1	1
9	1	1	0	0	0	0	0	0
10	2	0	0	0	2	0	2	−2
11	2	0	0	0	2	0	2	−1
12	2	0	0	0	2	0	2	0
13	2	0	0	0	2	0	2	1
14	2	0	0	0	2	0	2	2
15	0	0	0	0	0	0	0	0

block matrix form as

$$
\begin{pmatrix}
-\frac{1}{2}\lambda_1 \mathbf{1}_5 & \mathbf{0} & \mathbf{0} & \frac{1}{\sqrt{2}}\lambda_2 \mathbf{1}_5 & \mathbf{0} \\
\mathbf{0} & \frac{1}{2}\lambda_1 \mathbf{1}_3 & \mathbf{0} & \mathbf{0} & \mathbf{0} \\
\mathbf{0} & \mathbf{0} & \lambda_1 & \mathbf{0} & \frac{1}{\sqrt{2}}\lambda_3 \\
\frac{1}{\sqrt{2}}\lambda_2 \mathbf{1}_5 & \mathbf{0} & \mathbf{0} & \mathbf{0} & \mathbf{0} \\
\mathbf{0} & \mathbf{0} & \frac{1}{\sqrt{2}}\lambda_3 & \mathbf{0} & \mathbf{0}
\end{pmatrix} \quad (21)
$$

where $\mathbf{1}_N$ stands for the $N \times N$ unit matrix and $\mathbf{0}$ denotes appropriate $N \times M$ zero matrices. In this equation, λ_1 is the intra-state coupling constant for the ^3P atomic state, λ_2 is the inter-state coupling constant between ^3P and ^1D atomic states and λ_3 is the inter-state coupling constant between ^3P and ^1S atomic states. Note that we simplified the notation by changing the number of indices of the λ parameters when compared to eqn (4).

The strategy followed to fit the three λ_i parameters aims at reproducing the experimental levels of the sulfur atom.[21] In our model, the 5 asymptotic energies are obtained by diagonalization of the sum of the SO matrix and the three asymptotic energies of the Coulomb part. These three SO-free *ab initio* energies differ from the weighted average of the observed values[21] by at most 70 cm^{-1} due to inaccuracies in the *ab initio* computations. As a consequence, the optimization of the λ_i parameters was combined with the modification of the asymptotic energies of the Coulomb model in order to match with the experimental values. Experimental transition energies are 396.055 cm^{-1}, 573.64 cm^{-1}, 9238.609 cm^{-1} and 22179.954 cm^{-1}, respectively.[21] These numbers are (by construction) perfectly reproduced by our model.

It should be noted that the inter-state SO couplings expressed in the basis given in Table 2 do not vanish at large distances. These couplings mix different terms arising from the same electron configuration and having the same total angular momentum j_{SAr}. As a result, the physical states, characterized by the quantum number j_{SAr}, are described by linear combinations of the basis states of Table 2. To facilitate the matching process and to compute collision cross sections, a basis transformation must be performed to diagonalize the potential matrix at large distances.

IV. Results

A. Potential energy curves

The parameters of the Coulomb model of the potential energy surface (PES) are obtained by fitting the ansatz described in Section III B against the *ab initio* data (see Section III A). The exceptions are the dispersion parameters c_{6j}^D in eqn (14), which could be obtained more directly through a linear fit against the *ab initio* data on a double logarithmic scale. Since the dispersion term describes the shape of the long-range interaction to an accuracy beyond that of the underlying electronic structure (≤ 1 cm^{-1}), no higher order terms are considered in this domain.

Table 3 compares the long-range interaction coefficients thus obtained with those of ref. 5. In this earlier work, *ab initio* electronic energies were obtained using MOLPRO from MRCI+Q calculations in C_{2v} symmetry, with the aug-cc-pV5Z orbital basis. The energies were corrected for the basis set superposition error (BSSE) using the counterpoise procedure of Boys and Bernardi.[22] Once the MRCI wavefunctions for the nine electronic states had been determined, the matrix elements of the SO part of the Breit-Pauli Hamiltonian were calculated at each internuclear distance. The long-range interactions corresponding to the $1^1\Sigma^+$ state were independently calculated using a multipolar expansion of the electrostatic interaction operator, treated at the second order of perturbation theory. The resulting energies were matched at large distances with their MRCI counterpart.

The values obtained in the current calculation are about 10% larger than those reported in ref. 5. We infer that this comes from the different electronic structure, as well as from

Table 3 Comparison of equilibrium distances R_{min} given in bohr, well depths D_e in cm^{-1} and dispersion coefficients c_6 in hartree bohr^6 between present work and ref. 5

Symmetry	R_{min}	Ref. 5	D_e	Ref. 5	c_6	Ref. 5
$^3\Pi$	7.09	7.10	133	160	−96.4	−87.4
$^3\Sigma^-$	7.88	7.90	85	99	−107.5	−93.7
$1^1\Sigma^+$	6.08	6.20	289	264	−95.0	−88.5
$^1\Pi$	7.12	7.11	129	144	−98.5	−90.0
$^1\Delta$	7.82	7.80	90	101	−108.7	−94.7
$2^1\Sigma^+$	7.29	7.41	126	128	−95.0	−92.6

3726 | *Phys. Chem. Chem. Phys.*, 2025, **27**, 3722–3731

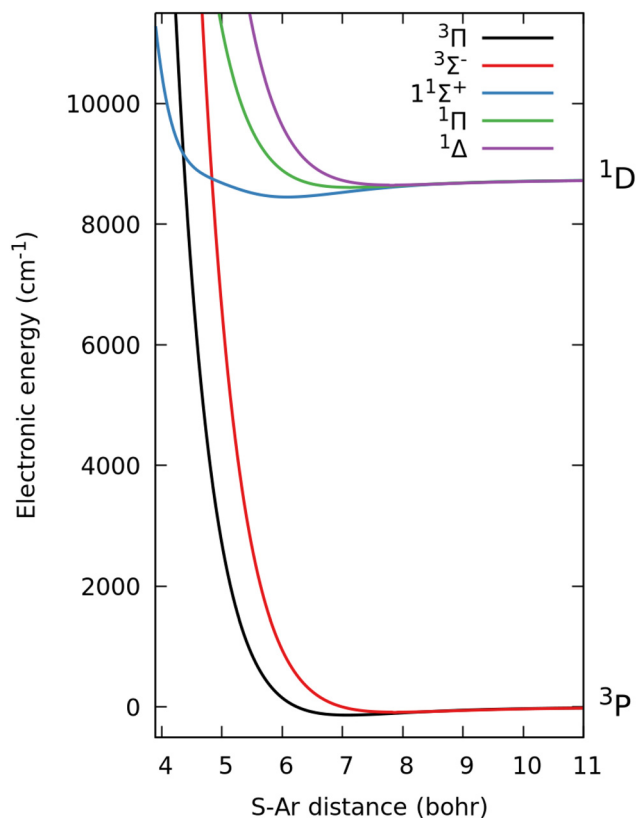This journal is © the Owner Societies 2025

Fig. 1 Adiabatic energies of the (SO-free) Coulomb model labelled according to $C_{\infty v}$ symmetry. The ^3P and ^1D asymptotic channels of sulfur are also indicated on the right. The *ab initio* energies visually coincide on the scale of the figure. Note that the $2^1\Sigma^+$ energy corresponding asymptotically to the ^1S state of sulfur is not shown.

the different methodology employed to obtain these coefficients. Our values for the well depths and equilibrium distances also subtly deviate from those reported in ref. 5. The largest difference in equilibrium distance is found to be 0.12 bohr for the two states of Σ^+ symmetry. The well depths obtained in the current work agree with those given in ref. 5 to within 30 cm^{-1}. The largest differences are obtained for the ground $^3\Pi$ (27 cm^{-1} shallower) and for the $1^1\Sigma^+$ (25 cm^{-1} deeper) curves. The total root mean square error (RMSE) achieved by the fit across all *ab initio* data points is 28 cm^{-1} including all adiabatic energies up to 1 eV above their respective dissociation energy. The RMSE is dominated by the error in the repulsive walls, with differences between model and *ab initio* data consistently ≤ 1 cm^{-1} for large ranges of R, for all considered states. Fig. 1 shows the energies of the Coulomb model corresponding to the ^3P and ^1D channels. The ^1S is about 22 000 cm^{-1} above the ^3P state (and thus not shown). On the scale of the figure, the *ab initio* energies are indistinguishable from the presented curves. The $1^1\Sigma^+$ state exhibits a characteristically "dented" shape between the minimum and the repulsive wall with a moderate slope. Due to this particular shape, the intersections of this curve with the two triplet states are extremely sensitive to minor changes in the electronic structure. These singlet–triplet intersections become avoided crossings

when the SO coupling is taken into account. The dented shape of the $1^1\Sigma^+$ state is caused by subtle nonadiabatic coupling effects with the $2^1\Sigma^+$ state. Indeed our model shows a strong coupling between these two electronic states especially for distances less than 6.5 bohr, where the coupling strength approaches the size of the energy gap between the adiabatic energies (on the eV scale). We thus infer that the exact shape of the $1^1\Sigma^+$ potential curve is extremely sensitive to the electronic structure calculation and especially to the convergence of the nonadiabatic coupling. This is a key limitation, as it is far more difficult to converge electronic wave function properties rather than the adiabatic energies.

Fig. 2 shows the adiabatic energies obtained from the full ERCAR potential model, including SO coupling. The asymptotic energies are split into 5 levels corresponding to Ar($^1S_0$) and S($^3P_{2,1,0}$, $^1D_2$, $^1S_0$). As outlined in Section III C, experimental transition energies for atomic sulfur are reproduced by construction. Note that the S–Ar adiabatic curves are labelled by their $\Omega = |M_{J_{SAr}}|$ quantum number as is common in spectroscopy. For $\Omega = 0^\pm$, the upper index denotes whether the state is odd or even with respect to reflections in a plane which contains the atoms.

At shorter inter-atomic distances, the $^3P_2$ level splits into $\Omega = 2, 1$ and 0^+ components with $\Omega = 2$ being the lowest curve (see Fig. 3). The $^3P_1$ level is composed of $\Omega = 1$ and $\Omega = 0^-$ curves while $^3P_0$ corresponds to the second $\Omega = 0^+$. Finally, the $^1D_2$ channel splits into another set of $\Omega = 2, 1, 0^+$ curves as shown in Fig. 4, while $^1S_0$ forms the fourth $\Omega = 0^+$. The curves of identical Ω form avoided crossings where the former $1^1\Sigma^+$ intersects with the $^3\Pi$ and $^3\Sigma^-$. In particular the $\Omega = 0^+$ curves present two avoided crossings at distances between 4 and 5 bohr. Fig. 4 shows the aforementioned avoided crossings in greater detail. It is of particular note that the lower-lying crossing nearly coincides with the dissociation energy of the $^1D_2$ channel, making it a dynamically accessible and extremely relevant feature of the surface. The horizontal line in Fig. 4 corresponding to the energy of the $^1D_2$ channel is drawn to emphasize
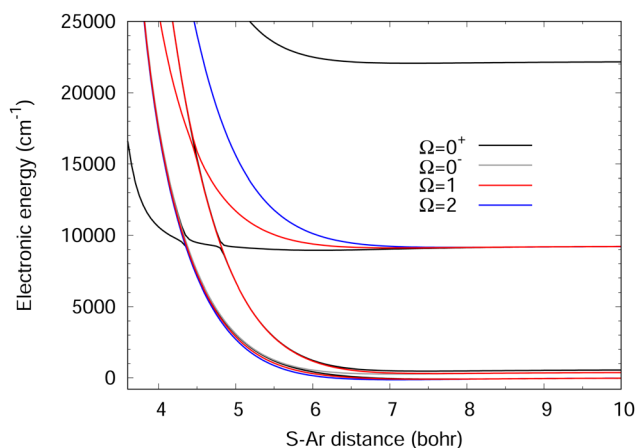

Fig. 2 Adiabatic potential curves over the full energy range. The S–Ar distance is given in bohr and the energies in cm^{-1}. Zero is defined as the asymptotic limit of the lowest curve.
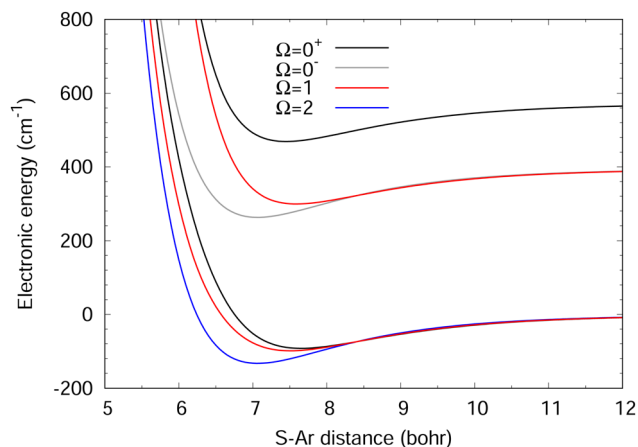
This journal is © the Owner Societies 2025

Phys. Chem. Chem. Phys., 2025, **27**, 3722–3731 | **3727**

Fig. 3 Zoom on the low energy part of the adiabatic potential curves. The S–Ar distance is given in bohr and the energies in cm^{-1}.
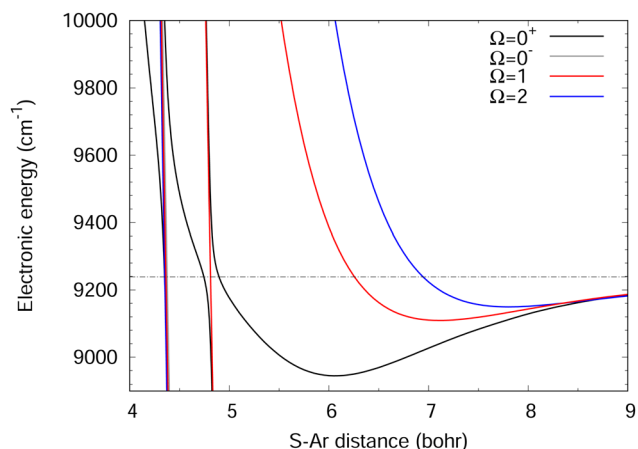

Fig. 4 Zoom on the energy range around the $^1D_2$ energy, indicated by the dashed horizontal line. The two avoided crossings of the $\Omega = 0^+$ curves (in black) are clearly visible at about 4.35 and 4.8 bohr.

this particularity. The second crossing, at a distance about half a bohr shorter and only 400 cm^{-1} higher in energy, is also expected to be dynamically reachable.

B. Scattering

In all the scattering calculations, the reduced mass of the S + Ar system is taken to be $\mu = 32377.6463$ a.u. Partial waves up to $J = 120$ were included. The basis transformation matrix that diagonalizes the inter-state SO couplings was obtained by diagonalizing the potential matrix at 5×10^7 bohr. For each partial wave and collision energy, the logarithmic derivative matrix was propagated from 3.6 bohr out to 60 bohr in steps of 0.003 bohr, where it was matched to the corresponding logarithmic derivative for the asymptotic solutions to give the scattering matrix **K**. Cross sections were calculated for collision energies up to 3000 cm^{-1}, and then used to compute energy-dependent rates as well as thermal rates up to 300 K. We have verified that the

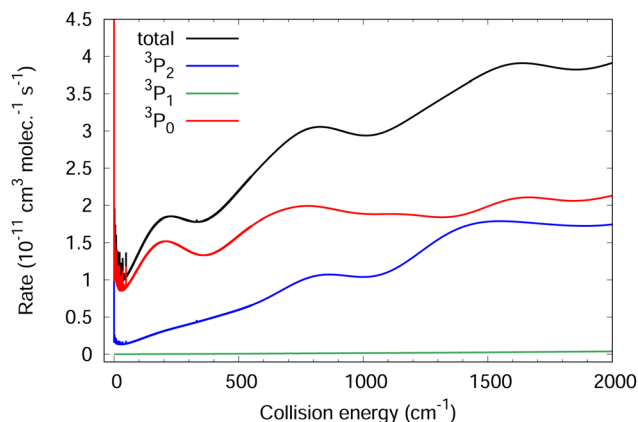**Fig. 5** Total and partial energy-dependent rate coefficients as a function of the collision energy relative to the initial $S(^1D_2)$ level.

results obtained are converged with respect to the number of partial waves, the step length and the matching radius.

In Fig. 5 we present the total energy-dependent rate coefficient, eqn (9), for the quenching process from the $S(^1D_2)$ level down to the ^3P multiplet. We also show the individual rates for quenching into the $^3P_{0,1,2}$ fine structure levels. Transitions into the $^3P_0$ level provide the largest contribution to the total quenching rate, although its relative importance compared to the contribution from the $^3P_2$ level diminishes as the collision energy (relative to the initial $S(^1D_2)$ level) increases. Quenching into the $^3P_1$ level is very small throughout the energy range considered. This can be attributed to the absence of any coupling between the $\Omega = 0^+$ component of the asymptotic $S(^1D_2)$ potential curve and the $\Omega = 0^-$ component of the $S(^3P_1)$ curve in the neighborhood of the relevant crossings, see Fig. 2–4. Populating the $^3P_1$ level hence requires changing Ω through Coriolis couplings (i.e. off-diagonal elements of the centrifugal potential in the BF basis), whose action has been shown to be very small for S + Ar.[5]

Resonances are discernable at collision energies below 60 cm^{-1}, as can be seen in Fig. 6 which provides a zoom on
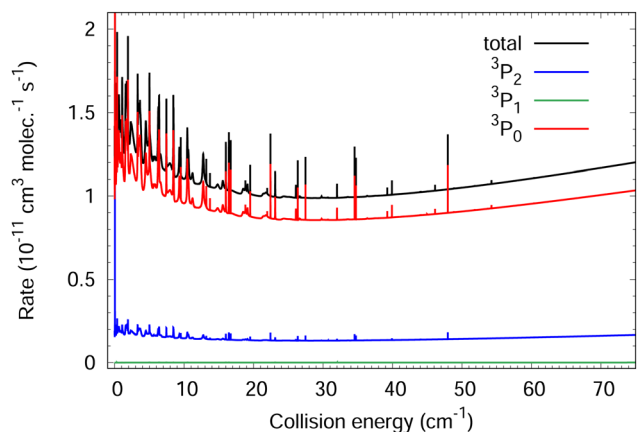

Fig. 6 Total and partial energy-dependent rate coefficients as a function of the collision energy in the resonance region close to threshold.

3728 | Phys. Chem. Chem. Phys., 2025, **27**, 3722–3731

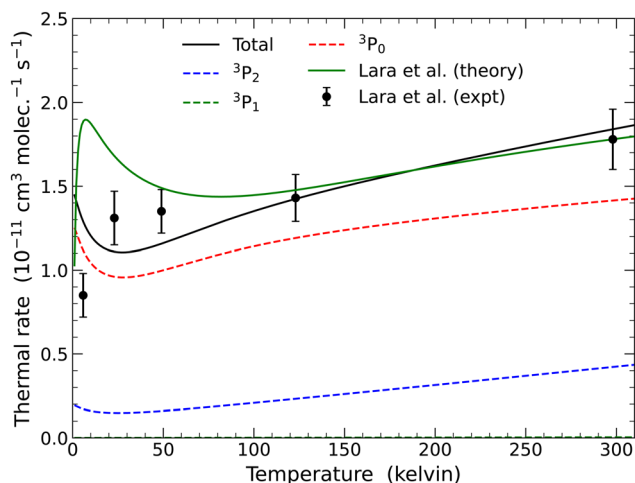This journal is © the Owner Societies 2025

Fig. 7 Total and partial thermal rate coefficients for quenching. The experimental data and the green curve labelled Lara *et al.* are from ref. 5.

this energy region. Most are associated with the $^1D_2 \rightarrow {}^3P_0$ transition simply because this is the dominant contribution at these energies. Occurring in different partial waves (J values), resonances are signatures of quasi-bound states supported by the effective potential in each channel resulting from the combination of the attractive well and the repulsive centrifugal barrier. The resulting potential landscape can then be quite tortuous due to the various avoided crossings in the adiabatic potential curves shown in Fig. 4. While the individual resonance structures themselves are quite narrow, they nevertheless have an important effect on the thermally averaged rates at low temperatures. It is therefore important to adequately resolve these resonances.

Comparing with the corresponding energy-dependent rates given in Fig. 6 of ref. 5 reveals a number of important differences. For collision energies above 500 cm^{-1}, the current total energy-dependent rate is consistently larger than that of ref. 5, the percentage differences reaching as much as 30%. In the resonance region shown in Fig. 6, however, the results of ref. 5 tend to be larger, for example by approximately 30% between 20 and 30 cm^{-1} where our total energy-dependent rate has a minimum. While it may appear that there are more resonances in the current results than in those of ref. 5, this is almost certainly due to the much finer energy grid used here to adequately resolve the resonance structure. The most striking differences occur in the partial energy-dependent rates into the $^3P_0$ and $^3P_2$ levels. In the earlier work, these partial rates as a function of collision energy cross near 110 cm^{-1}, so that at higher energies the main contribution comes from transitions into the $^3P_2$ level. The authors attributed this to a crossing of potential energy curves at 6.86 bohr (labelled as C3 in their work). In the current work, however, no such crossing occurs, so that the major contribution to the quenching process is always from transitions into the $^3P_0$ level. Indeed, at collision energies corresponding to temperatures in the vicinity of 296 K ($\sim$206 cm^{-1}), transitions into the $^3P_0$ and $^3P_2$ levels contribute roughly 82% and 17% respectively to the total energy-dependent rate.

In Fig. 7 we present the total and partial thermal rate coefficients, eqn (10), for temperatures from 5 to 300 K. The experimental and theoretical results from ref. 5 are also shown. The two experimental data points above 100 K are well reproduced by both calculations. Below 50 K, neither of the two theoretical thermal rates agree with the experimental data. While the earlier results overestimate the experimental values, with a maximum near 10 K, the current results underestimate them, displaying a minimum between 20 and 30 K. The sensitivity of the theoretical thermal rates is directly related to the fine details of the coupled potential curves used, as shown in Fig. 11 of ref. 5. We further infer that the position of the avoided crossing at the energy of the entrance channel is responsible for this. We also remark that the partial thermal rate at 296 K for transitions into the $^3P_0$ level accounts for approximately 77% of the total rate, close to the experimental estimation[6] of around 80%, while transitions into the $^3P_2$ level contribute roughly 23%. Comparing with the branching ratios for the energy-dependent rates, we see that the thermal averaging has slightly reduced the relative contributions from transitions into S($^3P_0$), enhancing those into S($^3P_2$).

Our branching ratios thus indicate a strong propensity for quenching into the $^3P_0$ fine structure level throughout the temperature range considered. A similar propensity was seen for quenching of O(^1D) by Ar,[9] which should not be surprising since oxygen lies just above sulfur in the periodic table. It is interesting to note that while the calculations in ref. 5 give similar values to ours for the total rate coefficient, their branching ratios are very different with a propensity for populating the $^3P_2$ level at 296 K. Despite the continuing discrepancy in the rate coefficients at low temperature, our results would thus appear to be a step in the right direction.

V. Conclusion

We have developed an accurate spin–orbit coupled diabatic potential model for the scattering of sulfur in its ground configuration with argon, and applied it to the study of electronic quenching of the S($^1D_2$) fine structure level. The states of interest are all fine structure states corresponding to the asymptotic limits S($^1D_2$) + Ar($^1S_0$) and S($^3P_{2,1,0}$) + Ar($^1S_0$). To account for nonadiabatic coupling effects the S($^1S_0$) + Ar($^1S_0$) asymptotic limit is also included in the model. Using the ERCAR approach, the coupled diabatic potential model relies on accurate SO-free *ab initio* data for the nine adiabatic energies of S + Ar, namely $^3\Sigma^-$, $^3\Pi$, $1^1\Sigma^+$, $^1\Pi$, $^1\Delta$ and $2^1\Sigma^+$. These correlate to three asymptotic energies corresponding to the ^3P, ^1D and ^1S states of sulfur. When the spin–orbit (SO) interaction is included, 15 fine structure states are obtained. The ERCAR approach allows us to use the experimental SO energies of atomic sulfur as well as an asymptotic diabatic basis to build a fully coupled 15 × 15 diabatic representation of the interaction potential for S + Ar at all inter-atomic distances. The advantages of ERCAR are its high accuracy and low computational demand, recovering geometry-dependent spin–orbit information while

This journal is © the Owner Societies 2025

Phys. Chem. Chem. Phys., 2025, **27**, 3722–3731 | **3729**

being able to keep *ab initio* calculations at the SO-free level for all distances except for at most one point at infinite separation. Alternatively atomic spin–orbit data can be taken from experiment instead, forgoing the need of SO calculations entirely. In the resulting model, the spin–orbit interaction is intrinsically a function of the inter-atomic distance.

The coupled surfaces thus obtained have been used to compute the energy-dependent and thermal rates for the quenching of $S(^1D_2)$ by Ar. Since the underlying basis is constructed using eigenstates of the electronic angular momentum, the close coupling equations follow directly. Partial waves up to total angular momentum $J = 120$ have been used to compute quenching cross sections at collision energies up to 3000 cm^{-1} and hence thermal rates from 1 to 300 K. The results above 100 K are in good agreement with those of a previous theoretical and experimental study.[5] At low temperatures however the discrepancy between the theoretical and the experimental data remains. In contrast to the earlier work, the computed branching ratio at 296 K for transitions into the $^3P_0$ fine structure level is in good agreement with the experiment of Stout *et al.*[6]

The S + Ar system has a delicate electronic structure with multiple avoided crossings. We infer that at least the position of one of these is responsible for the high sensitivity of the scattering results to fine details of the potential model. Since our diabatic PES reproduces *ab initio* data well, we conclude that inaccuracies in the underlying data are a dominant source of error, rather than the surface itself. Further work is clearly necessary in order to reconcile theory and experiment, particularly in view of the different trends shown by the two calculations and the experiment as the temperature approaches 0 K. On the theory side, *ab initio* calculations going beyond those used here are clearly necessary, while additional experimental work would help confirm and extend the existing measurements.

Data availability

All essential data is already provided within the manuscript. Further data is available from the author upon reasonable request.

Conflicts of interest

There are no conflicts to declare.

Acknowledgements

References

1 W. H. Breckenridge and H. Taube, Some Reactions of Ground State (^{3}P) and Electronically Excited (^{1}D) Sulfur Atoms, *J. Chem. Phys.*, 1970, **53**(5), 1750–1767.

2 K. Schofield, Critically Evaluated Rate Constants for Gaseous Reactions of Several Electronically Excited Species, *J. Phys. Chem. Ref. Data*, 1979, **8**(3), 723–798.

3 G. Black and L. E. Jusinski, Rate coefficients for $S(^1D)$ removal at 300 K, *J. Chem. Phys.*, 1985, **82**, 789–793.

4 C. Berteloite, M. Lara, A. Bergeat, S. D. Le Picard, F. Dayou and K. M. Hickson, *et al.*, Kinetics and Dynamics of the $S(^1D_2) + H_2 \rightarrow SH + H$ Reaction at Very Low Temperatures and Collision Energies, *Phys. Rev. Lett.*, 2010, **105**, 203201.

5 M. Lara, C. Berteloite, M. Paniagua, F. Dayou, S. D. Le Picard and J. M. Launay, Experimental and theoretical study of the collisional quenching of $S(^1D)$ by Ar, *Phys. Chem. Chem. Phys.*, 2017, **19**, 28555–28571.

6 J. E. Stout, B. K. Andrews, T. J. Bevilacqua and R. B. Weisman, Cars observation of the fine structure population inversion from atomic quenching: $S(^1D) + Ar \rightarrow S(^3P_0) + Ar$, *Chem. Phys. Lett.*, 1988, **151**, 156–160.

7 P. J. Dagdigian, M. H. Alexander and J. Kłos, Theoretical investigation of the dynamics of O ($^1D \rightarrow ^3P$) electronic quenching by collision with Xe, *J. Chem. Phys.*, 2015, **143**, 054306.

8 L. A. Garofalo, M. C. Smith, P. J. Dagdigian, J. Kłos, M. H. Alexander and K. A. Boering, *et al.*, Electronic quenching of O (^1D) by Xe: Oscillations in the product angular distribution and their dependence on collision energy, *J. Chem. Phys.*, 2015, **143**, 054307.

9 D. Nuñez-Reyes, J. Kłos, M. H. Alexander, P. J. Dagdigian and K. M. Hickson, Experimental and theoretical investigation of the temperature dependent electronic quenching of O (^1D) atoms in collisions with Kr, *J. Chem. Phys.*, 2018, **148**, 124311.

10 E. C. G. Stückelberg, Theorie der unelastischen Stösse zwischen Atomen, *Helv. Phys. Acta*, 1932, **5**, 369.

11 N. Weike, A. Viel and W. Eisfeld, Hydrogen – iodine scattering: I. Development of an accurate spin–orbit coupled diabatic potential energy model, *J. Chem. Phys.*, 2023, **159**, 244119.

12 N. Weike, W. Eisfeld, K. M. Dunseath and A. Viel, Hydrogen – iodine scattering: II. Rovibronic analysis and collisional dynamic, *J. Chem. Phys.*, 2024, **161**, 014302-118.

13 H. Ndome, R. Welsch and W. Eisfeld, A New Method to Generate Spin-Orbit Coupled Potential Energy Surfaces: Effective Relativistic Coupling by Asymptotic Representation, *J. Chem. Phys.*, 2012, **136**, 034103.

14 H. Ndome and W. Eisfeld, Spin-Orbit Coupled Potential Energy Surfaces and Properties Using Effective Relativistic Coupling by Asymptotic Representation, *J. Chem. Phys.*, 2012, **137**, 064101.

3730 | *Phys. Chem. Chem. Phys.*, 2025, **27**, 3722–3731

This journal is © the Owner Societies 2025

15 N. Wittenbrink, H. Ndome and W. Eisfeld, Toward Spin-Orbit Coupled Diabatic Potential Energy Surfaces for Methyl Iodide Using Effective Relativistic Coupling by Asymptotic Representation, *J. Phys. Chem. A*, 2013, **117**(32), 7408–7420.

16 N. Wittenbrink and W. Eisfeld, An improved spin-orbit coupling model for use within the effective relativistic coupling by asymptotic representation (ERCAR) method, *J. Chem. Phys.*, 2017, **146**(14), 144110.

17 N. Wittenbrink and W. Eisfeld, Extension of the Effective Relativistic Coupling by Asymptotic Representation (ERCAR) approach to multi-dimensional potential energy surfaces: 3D model for CH₃I, *J. Chem. Phys.*, 2018, **148**, 094102.

18 N. Weike, E. Chanut, H. Hoppe and W. Eisfeld, Development of a Fully Coupled Diabatic Spin-Orbit Model for the Photodissociation of Phenyl Iodide, *J. Chem. Phys.*, 2022, **156**, 224109.

19 J. M. Launay, Molecular collision processes. I. Body-fixed theory of collisions between two systems with arbitrary angular momenta, *J. Phys. B:At., Mol. Phys.*, 1977, **10**(18), 3665.

20 H. J. Werner, P. J. Knowles, *et al.* MOLPRO 2009.1 is a package of *ab initio* programs. Stuttgart, Germany: see **https://www.molpro.net**.

21 Y. Ralchenko, A. E. Kramida, J. Reader and NIST ASD Team, NIST Atomic Spectra Database (version 3.1.5). Available: **https://physics.nist.gov/asd3**; 2008.

22 S. F. Boys and F. Bernardi, The calculation of small molecular interactions by the differences of separate total energies. Some procedures with reduced errors, *Mol. Phys.*, 1970, **19**, 553–566.

This journal is © the Owner Societies 2025

Phys. Chem. Chem. Phys., 2025, **27**, 3722–3731 | **3731**